

Major Tissue Contrast Enhancement in Breast MRI Using Constrained Energy Minimization Method

* Sheng-Chih Yang and Dong-Yuan Wu

Abstract

Among the most recent techniques of breast imaging modalities, a great attention is being paid to breast magnetic resonance imaging (MRI). Since the contrast-enhanced breast MRI acquired by contrast injection has been shown to be very sensitive in the detection of breast cancer. However, besides the discomfort of injection, the complexity of the contrast injection procedure is time-consuming and causes consumption of medical resources. This paper, therefore, adopted a spectral signature detection technology, the constrained energy minimization (CEM) method, on an arranged multi-spectral mixed-pixel image, which can successfully present the results as high-contrast images and classify breast MRIs into major tissues from four bands of non-injected (or non-contrast) breast MRIs. Finally, the generated high-contrast images are expected to be another option other than the contrast injection in the diagnosis. A series of experiments using phantom and real MRIs were conducted, and the results were compared with those of commonly-used c-means (CM) method, another rival, Kalman Filter-based Linear Mixing (KFLM) method and presently-used dynamic contrast-enhanced (DCE) breast MRIs for performance evaluation. After comparison with the CM, KFLM algorithm and DCE breast MRIs, the experimental results showed that the high contrast images generated by the spectral signature detection technology, the CEM, had a superior quality.

Keywords: contrast enhancement, breast MRI, breast cancer screening, constrained energy minimization method, tissue classification.

1. Introduction

Breast magnetic resonance imaging (MRI) is a mature technique that is ready for broad clinical use. Contrast-enhanced breast MRI has been shown to have a high sensitivity for the detection of breast cancer compared with that of conventional methods (mammography and ultrasound), with reported sensitivity of MRI for detection of invasive breast

cancer approaching 100% [1,2]. When performing MRI, three parameters, T1, T2, and PD, are usually applied to generate a multi-spectral image sequence that converts tissue variation into contrast in the images. For contrast enhancement, breast MRI is imaged several times in different sequences after the injection of a paramagnetic contrast agent. The pathophysiologic basis of contrast-enhanced breast MRI is based on the hypothesis that after injection of contrast agent, abnormalities enhance more than normal tissues due to neoangiogenesis, increasing local perfusion and capillary diffusion rates of malignant lesions [3]. However, the procedure of injection of contrast is more time-consuming and causes a lot of consumption of medical resources. Moreover, in a few cases with serious renal deficiencies, the association of gadolinium-based contrast used in MRI is associated with development of nephrogenic systemic fibrosis [4].

Based on these considerations, this study proposes an MRI classification and detection technology based on the spectral feature correlation among breast MRI sequences, called the constrained energy minimization (CEM) developed in previous studies [5,6] to classify breast MRIs into four high-contrast tissue-separated images. With this proposed scheme, there is a chance that we can do away with contrast injection for contrast enhancement. The CEM method is derived from the minimum variance distortion-less response (MVDR) approach based on the assumption that breast MRI contains multiple object signatures (i.e., fatty tissue, glandular tissue, tumor mass and muscle). In the MVDR, signal arrival from a desired direction is generally assumed to be known a priori. Then it designs an adaptive filter to pass through the desired signal using a unity filter constraint (i.e., scalar 1) while the filter output variance (i.e., energy) is minimized. In MRI classification, the desired direction of signal arrival is interpreted by the CEM filter as the direction pointed by a particular object pixel vector. Therefore, all the pixel vectors pointing to the same direction will belong to the same pattern class and will be passed by the CEM filter with a unity constraint while the energies (i.e., vector lengths) of pixel vectors pointing to other directions will be minimized [7].

One advantage of the CEM method over all traditional classification techniques and KFLM method is that it was designed on the premise that no background information is required for the target detection. The CEM filter classifies an object in an unknown image background of MR image sequence by constraining its vector direction while minimizing the effects resulting from other directions. This advantage is

*Corresponding Author: Sheng-Shih Yang

(E-mail: scyang@ncut.edu.tw).

Department of Computer Science and Information Engineering,
National Chin Yi University of Technology, Taichung 41170,
Taiwan

particularly significant when the desired targets are present in an image with complicated background that involves many unknown and unidentified targets which are not of our interest. On the other hand, the CEM is a spectral-based technique which does not rely its classification on object shapes. Consequently, the CEM may be more effective in soft objection classification than classical spatial analysis-based image processing classification techniques which utilize sample spatial information and correlation.

In order to validate our proposed method, CEM, computer-simulated phantoms were first used for quantitative analysis and evaluation of efficiency in a comparison with CM and KFLM methods. The reason for selecting the CM method for comparative purposes is twofold: first, it allows us to generate background signatures in an unsupervised manner for classification; second, it is basically a spatial-based pattern classification technique. Moreover, the reason for selecting the KFLM method for comparison is that its experimental results indicate the good performance of the spectral signature detection in our previous work [8]. Finally, real breast MRI taken before and after the contrast injection with four different parameters is also used to evaluate the feasibility of this technique in medical and clinical applications.

The organization of this paper is as follows. In Section II, the classification of an MR image sequence using CEM is formulated. Than another rival -- KFLM is described in Section III, and the modified version of the CM method implemented in this study is discussed briefly in Section IV. Section V details a set of experiments conducted to evaluate the performance of the CEM in MR classification, and also includes a comparison of the results of contrast-injected breast MRIs and those produced by the FFLM, CM method. Concluding remarks are presented in Section VI.

2. Constrained Energy Minimization (CEM) Approach

Let L be the number of spectral bands (channels) used to acquire MR image sequences. In this case, an MR image sequence is actually a collection of co-registered L spectral bands. Therefore, an i -th image pixel in an MR image sequence can be considered as a L -dimensional pixel vector, denoted by $r_i = (r_{i1}, r_{i2}, \dots, r_{iL})^T$ where r_{ij} represents the pixel of the i -th pixel vector in the j -th spectral band. Suppose that $\{r_1, r_2, \dots, r_N\}$ is the set of all image pixels in an MR image sequence where N is the total number of pixels in the image. Let d be the spectral signature of an object of interest. The goal is to design an FIR linear filter specified by an L -dimensional vector $w = (w_1, w_2, \dots, w_L)^T$ that passes the desired signature d by constraining its direction while minimizing its output energy that are caused by signal source vectors with directions other than the constrained direction.

More specifically, let y_i denote the output of the designed FIR filter resulting from the i -th MR image pixel r_i . Then y_i can be expressed by

$$y_i = \sum_{l=1}^L w_l r_{il} = w^T r_i = r_i^T w \quad (1)$$

The average filter output energy resulting from $\{r_1, r_2, \dots, r_N\}$ is given by

$$\frac{1}{N} \left[\sum_{i=1}^N y_i^2 \right] = \frac{1}{N} \left[\sum_{i=1}^N (r_i^T w)^T r_i^T w \right] = w^T \left(\frac{1}{N} \left[\sum_{i=1}^N r_i r_i^T \right] \right) w = w^T R_{L \times L} w \quad (2)$$

where $R_{L \times L} = \frac{1}{N} \left[\sum_{i=1}^N r_i r_i^T \right]$ is the auto-correlation sample matrix of the MR image sequence. Therefore, the CEM filter is the one solving the following linearly constrained optimization problem

$$\min \{w^T R_{L \times L} w\} \quad \text{subject to} \quad d^T w = 1 \quad (3)$$

The solution to Eq. (3) is given in [5,6] by

$$w^* = \frac{R_{L \times L}^{-1} d}{d^T R_{L \times L} d} \quad (4)$$

Substituting the optimal weight given by Eq. (4) for w in Eq. (1) yields in the CEM filter which implements a detector, $\delta_{CEM}(r)$ on an image pixel vector r and is given by

$$\delta_{CEM}(r) = (w^*)^T r = \left(\frac{R_{L \times L}^{-1} d}{d^T R_{L \times L} d} \right)^T r = \frac{d^T R_{L \times L}^{-1} r}{d^T R_{L \times L}^{-1} d} \quad (5)$$

As we can see from Eq. (5), when $r = d$, $\delta_{CEM}(d) = 1$ which satisfies the constraint in Eq. (3). In this case, the r is considered to be the desired object pixel and will be extracted by the CEM filter. Despite that the primary task of the CEM filter is object detection, as demonstrated in the experiments it can perform as a classifier by detecting different types of objects, one at a time. In this case, separate images are produced for each type of targets.

A comment is noteworthy. The value of $\delta_{CEM}(r)$ resulting from Eq. (5) represents the estimated amount of the abundance fraction of the object signature d contained in the image pixel r . Therefore, unlike most spatial-based classification methods which can be considered as label (class)-assignment techniques, the CEM filter detects a desired object by estimating its abundance fraction using Eq. (5). As a result, the image generated by the CEM filter is generally gray scale where the gray level value of each image pixel reflects the detected amount of the abundance fraction of the desired object present in the pixel. The object detection is

then performed based on the resulting gray scale image and classification is carried out by detecting the desired objects in separate images.

3. Kalman Filter-based Linear Mixing (KFLM) Method

In order to evaluate the performance of the CEM approach, the KFLM method is used for a comparative analysis since it has indicated the promising possibilities in our previous work. The KFLM applies the Kalman filter on the linear spectral mixture model of breast MRIs based on the assumption that breast MRIs contains multiple object signatures (i.e., fatty tissue, glandular tissue, tumor mass and muscle) with their complete knowledge; each MRI pixel is then regarded as a model construed by linear mixing of these object signatures [8].

3.1 Linear Spectral Mixture Model

A breast MRI can be regarded as a three-dimensional image where the third dimension is a spectral dimension specified by TR/TE parameters, in which each pixel is actually a column vector and can be modeled by linear mixing. It is assumed that there are p spectrally-distinct substances $\{\mathbf{m}_1, \mathbf{m}_2, \dots, \mathbf{m}_p\}$ contained in the image, where $\mathbf{r}(x,y)$ describes the image pixel vector represented by a $l \times 1$ column vector and l is the number of spectral bands at position (x,y) . Let \mathbf{M} be a $l \times p$ signature matrix denoted by $[\mathbf{d}_1 \mathbf{d}_2 \dots \mathbf{d}_p]$, where \mathbf{d}_j is a $l \times 1$ column vector representing the spectral signature of the j th substance \mathbf{m}_j in pixel vector \mathbf{r} . It also assumed that $\boldsymbol{\alpha}(x,y)$ is a $p \times 1$ column vector associated with \mathbf{M} , which is defined as $\boldsymbol{\alpha} = (\alpha_1 \alpha_2 \dots \alpha_p)^T$, where α_j represents the value of \mathbf{d}_j , the j th signature in pixel vector \mathbf{r} . Lastly, \mathbf{r} can be described as follows by the linear mixing model:

$$\mathbf{r}(x,y) = \mathbf{M}\boldsymbol{\alpha}(x,y) + \mathbf{n}(x,y) \quad (6)$$

where \mathbf{n} is a $l \times 1$ column vector and is generated as additive noise or measurement error.

3.2 Kalman Filter

The complete KFLM is composed of the linear mixing model of Eq. (6) and the abundance equation of the Kalman filter, as follows:

$$\boldsymbol{\alpha}(k+1) = \Phi(k+1,k)\boldsymbol{\alpha}(k) + \mathbf{u}(k) \quad (7)$$

where k replaces the position (x,y) in Eq. (6), representing the discrete instant of time at which the pixel is processed. Vector $\boldsymbol{\alpha}(k)$ represents the value of abundance at time k , $\Phi(k+1,k)$ is a known $p \times p$ state transition matrix that describes the change in abundance from time k to $k+1$, and, $\mathbf{u}(k)$ is a zero-mean $p \times 1$ abundance noise vector independent of $\boldsymbol{\alpha}(k)$, generated by the white process with a covariance matrix given by

$$E[\mathbf{u}(k)\mathbf{u}(m)^T] = \mathbf{Q} = \sigma_2^2 \delta_{km} \mathbf{I}_{p \times p} \quad (8)$$

where σ_2^2 is the variance of the abundance noise vector, δ_{km} is Kronecker's notation, given by

$$\delta_{km} = \begin{cases} 1, & k = m \\ 0, & k \neq m \end{cases}$$

and matrix $\mathbf{I}_{p \times p}$ is a $p \times p$ identity matrix. Based on the discrete-time Kalman filtering notation at discrete time k , Eq. (6) is modified as

$$\mathbf{r}(k) = \mathbf{M}(k)\boldsymbol{\alpha}(k) + \mathbf{n}(k) \quad (9)$$

where vector $\mathbf{r}(k)$ is the observed pixel at time k , and $\mathbf{M}(k)$ is a known signature matrix at time k . The zero-mean measurement noise in Eq. (6) is represented as $\mathbf{n}(k)$, which is generated by the white process with a covariance matrix given by

$$E[\mathbf{n}(k)\mathbf{n}(m)^T] = \mathbf{R} = \sigma_1^2 \mathbf{I}_{l \times l} \delta_{km} \quad (10)$$

The purpose of the KFLM is to obtain the minimum mean-squared estimation of abundance state $\boldsymbol{\alpha}(k)$ with observed data $\mathbf{r}(k)$. Using knowledge of the predicted $\boldsymbol{\alpha}(k)$, we can classify and detect pixel $\mathbf{r}(k)$. Assuming $\hat{\boldsymbol{\alpha}}(k+1|k)$ is the minimum mean-squared estimation of $\boldsymbol{\alpha}(k+1)$ obtained from the previously observed value $\mathbf{r}(j)$, with j from 1 to k , and, then, $\hat{\boldsymbol{\alpha}}(k|k)$ and $\hat{\boldsymbol{\alpha}}(k|k-1)$ can be deduced by analogy. We further define $\mathbf{P}(k|k)$ as the error covariance matrix at time k from the previously observed $\mathbf{r}(j)$, with j from 1 to k , and $\mathbf{P}(k+1|k)$ as the prediction error covariance matrix at time $k+1$. Then, the KFLM is computed recursively to obtain the abundance vector of each pixel as the result of the classification. For more details on the implementation of the Kalman filter, refer to [9,10].

4. C-means (CM) Method

As opposed to the CEM and KFLM approaches, which only classify objects of interest, the CM method classifies all MR image pixel vectors, including background pixel vectors, into pattern classes. In order to make a fair comparison, the CM method used here includes in its clustering procedure the same knowledge of objects of interest that is required by the CEM and KFLM approaches. The CM method implemented in this paper for experiments is a modified version of the commonly-used CM method, which is also referred to as ISODATA in [11,12].

Let the spectral signatures of p objects of interest be denoted by $\{\mathbf{d}_i\}_{i=1}^p$, where \mathbf{d}_i is the spectral signature of the i -th object. The implementation of the CM method is described in detail below.

Modified CM Method

- 1). Determine the number of pattern classes, $c \geq p$, and let $\{\boldsymbol{\mu}_i\}_{i=1}^c$ be their corresponding class means.
- 2). Initialization: Let $k = 0$ and the first p class means are fixed at $\boldsymbol{\mu}_i^{(0)} = \mathbf{d}_i$. All class means $\boldsymbol{\mu}_i^{(0)}$, $i > p$ are selected. $\{\mathbf{d}_i\}_{i=1}^p$ must be in a different class.
- 3). At the k -th iteration, compute the distance of each sample pixel vector from all class means, $\boldsymbol{\mu}_i^{(k)}$ for $1 \leq i \leq c$ and assign the sample vector to the class whose mean is the shortest distance from the sample vector.
- 4). For each class i with $p \leq i \leq c$, recompute the class mean by averaging the sample vectors in the class, denoted by $\hat{\boldsymbol{\mu}}_i^{(k)}$. Let $k \leftarrow k + 1$, $\boldsymbol{\mu}_i^{(k)} = \mathbf{d}_i$, $1 \leq i \leq p$ and $\boldsymbol{\mu}_i^{(k)} \leftarrow \hat{\boldsymbol{\mu}}_i^{(k)}$ for $p \leq i \leq c$.
- 5). If any class mean changes in the set $\{\boldsymbol{\mu}_i^{(k)}\}_{i=p}^c$, go to step 3.

It should be noted that knowledge of $\{\mathbf{d}_i\}_{i=1}^p$ is required a priori. Therefore, the first p class means are fixed during iterations; however, the class means, $\{\boldsymbol{\mu}_i^{(k)}\}_{i=p}^c$, are regenerated at each iteration by the CM method in a supervised manner using the minimum distance as a criterion. These generated class means are considered to be signatures of unknown signal sources, which are not provided by prior knowledge and may include background signatures.

5. Experimental Results

This section describes a series of experiments based on computer-simulated phantoms and real breast MRIs. Using computer-simulated phantoms allows us to carry out quantitative research and error analysis on the CEM, while real breast MRIs are used to evaluate the effectiveness and practicality of the CEM in medical clinical diagnosis.

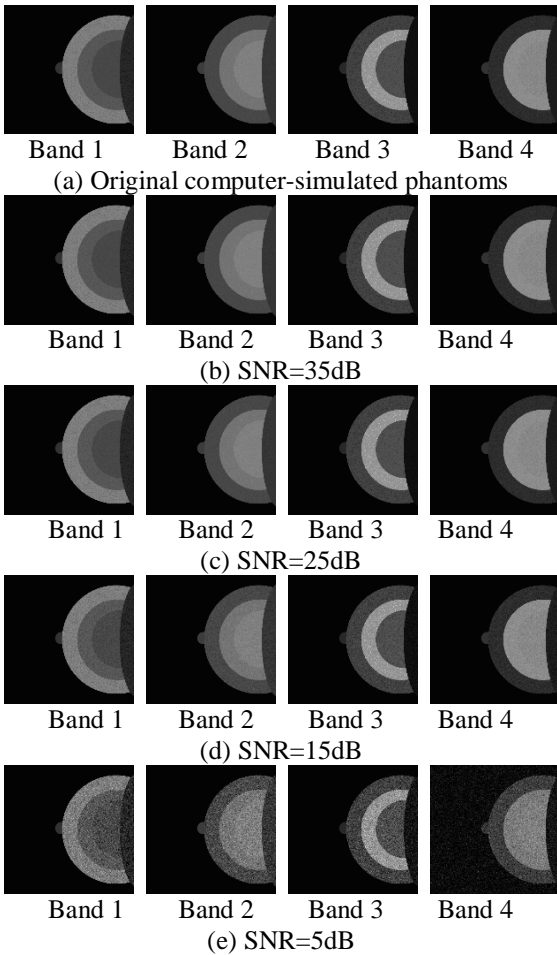
5.1 Computer-simulated phantoms evaluation

In this subsection, we utilize a series of computer-simulated phantoms for quantitative analysis, efficiency evaluation and performance comparison between the CEM, KFLM and CM methods. The number of classes in the CM method is set at 5, representing the five classes of major tissues, which are fatty tissue, glandular tissue, tumor, muscle and background in breast MRI. The phantoms generated by the computer in four different bands, corresponding to four real MRI sequences, are shown in Fig. 1, at 419×419 in size. The four semicircles represent four areas of breast tissues, which from left to right are nipple, fatty tissue, glandular tissue and tumor, while the semi-ellipse in the rightmost represents an area of muscles. For a better reflection of the characteristics of real breast MRIs, the gray level values in the tissue area in each band of the computer-simulated phantoms correspond to the average and variance of each tissue area in real breast MRIs, which were verified by three experienced radiologists, as shown in Fig. 5. In our phantoms, texture features are not simulated. The texture features could be simply clipped from each real tissue area and paste to phantoms for more realistic simulations of the anatomy. Although the texture is an important feature for many single-spectrum feature extraction algorithms, its influence and effect are limited to the multi-spectral algorithms. Instead, more emphasis on multi-spectral algorithms especial for CEM is the relative relationship between the spectrums, which has been simulated in our phantoms using the average and variance of each tissue area in real breast MRIs.

Table 1 tabulates the average gray level values and variances for the major tissues in each band of the computer-simulated phantoms, where Bands 1~4 correspond to sequences Flash, T1, T2 and PD respectively. Due to the fact that noises may be caused by the magnetic field of static, radio frequency and gradient or other factors during acquisition of the MRI, zero-mean Gaussian noise was added to the original phantom images in Fig. 1(a) so as to achieve different levels of signal-to-noise ratio (SNR), ranging from 35dB to 5dB, as shown in Figs. 1(b)-(e). These phantoms with different levels of signal-to-noise ratios also serve to illustrate the proposed CEM technique and demonstrate its advantages.

Table 1: Average gray level values and variances used for the four bands of the computer-simulated phantoms in Fig. 1.

MRI sequence	Back Ground	Tissue								
		Fatty		Glandular		Tumor		Muscle		
		average	variance	average	variance	average	variance	average	variance	
Band 1	Flash	3	125	101~138	87	71~92	72	67~78	38	14~47
Band 2	T1	3	72	66~78	116	110~126	128	119~135	54	50~64
Band 3	T2	3	65	40~78	151	140~206	78	50~85	15	9~18
Band 4	PD	3	45	31~54	141	130~152	136	124~151	29	26~40

**Figure 1: Computer-simulated phantoms of the four bands with different signal-to-noise ratios (SNR).**

5.1.1. Abundance Percentage Thresholding Method

In the application of the CEM and KFLM approaches to these simulated images, the signature matrix \mathbf{M} is assigned four objects of interest, which are fatty tissue, glandular tissue, tumor and muscle. As mentioned above, the images generated by the CEM and KFLM have gray level values that are in proportion to the detected abundance fraction of \mathbf{M} .

On the other hand, the CM method is a classical class-labeling process in which each data sample vector is assigned to only one class. Therefore, images generated by the CM method are classification images, rather than gray-scale images as generated by the CEM and KFLM approaches. To carry out the quantitative study and compare the results with those of the CM method, we converted the abundance fractional images generated by the CEM and KFLM into binary images; thus, we adopted the method proposed in [13], which uses the abundance fraction percentage as the cut-off threshold value for such a conversion. We first normalized the abundance fraction of the image with the range of [0,1]. More specifically, let \mathbf{r} be the pixel vector of the image and $\hat{\alpha}_1(\mathbf{r}), \hat{\alpha}_2(\mathbf{r}), \dots, \hat{\alpha}_p(\mathbf{r})$ be the estimated abundance fractions of $\alpha_1, \alpha_2, \dots, \alpha_p$ in \mathbf{r} ; then the normalized abundance fraction of each estimated abundance fraction $\hat{\alpha}_j(\mathbf{r})$ can be obtained by

$$\tilde{\alpha}_j(\mathbf{r}) = \frac{\hat{\alpha}_j(\mathbf{r}) - \min_r \hat{\alpha}_j(\mathbf{r})}{\max_r \hat{\alpha}_j(\mathbf{r}) - \min_r \hat{\alpha}_j(\mathbf{r})} \quad (11)$$

Assume that $a\%$ is the cutoff abundance fraction threshold value; i.e., if the normalized abundance fraction of the pixel vector is greater than or equal to $a\%$, then the pixel will be detected as a desired object pixel and set to "1"; otherwise, it will be set to "0", meaning it is not detected as a desired object pixel. In the sequel, using this cutoff threshold value to threshold a fractional abundance image will be referred to as the $a\%$ thresholding method. Fig. 3 shows the Correct Classification Rates (Rc) curves of tumor classification in the KFLM for the case of SNR = 5dB, 15dB, 25dB and 35dB, where the cutoff threshold values of $a\%$ were chosen to be 5%, 10%, 15%, 20%, 25%, 30%, 35%, 40%, 45%, 50%, 55%, 60%, 65%, 70%, 75%, 80%, 85%, 90%, 95% and 100% and the Correct Classification Rates (Rc) was as defined in Eq. (16). From Fig. 2(a), we can see that the CEM has an optimal Rc when $a\% = 45\%$ for both SNR = 25dB and 35dB, $a\% = 50\%$ for SNR = 15dB, and $a\%$

= 55% for SNR = 5dB. Comparing Fig. 2(a) with Fig. 2(b), it can also be seen that CEM has better performance than KFLM.

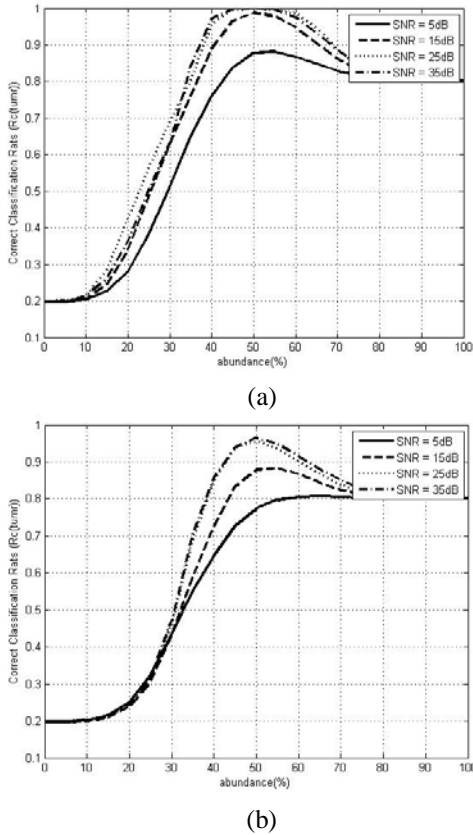


Figure 2: Correct Classification Rates (Rc) curves of tumor classification in (a) CEM (b) KFLM.

5.1.2. Receiver Operating Characteristic (ROC) Curve Analysis

Using the abovementioned a% thresholding method, we were able to calculate the number of detected pixels in the generated fractional abundance image. This subsection further utilizes the ROC (Receiver Operating Characteristic) curve for the analysis based on the gradually increasing a%. First, let $\{d_i\}_{i=1}^p$ be a set of objects of interest for classification; then, we define $N(d_i)$ as the total number of pixels specified by the i-th object signature d_i , $ND(d_i)$ as the number of pixels specified by the i-th object signature d_i and actually detected as the d_i , and $NF(d_i)$ as the number of false alarm pixels that are not specified by the object signature d_i but are detected as d_i . Using the definitions of $N(d_i)$, $ND(d_i)$ and $NF(d_i)$, we further define the detection rate $RD(d_i)$ and the false alarm rate $RF(d_i)$ for a particular object signature d_i by

$$R_D(d_i) = \frac{N_D(d_i)}{N(d_i)} \tag{12}$$

$$R_F(d_i) = \frac{N_F(d_i)}{N - N(d_i)} \tag{13}$$

and the mean detection rate RD and mean false alarm rate RF for all object signatures by

$$R_D = \sum_{i=1}^p R_D(d_i) p(d_i) \tag{14}$$

$$R_F = \sum_{i=1}^p R_F(d_i) p(d_i) \tag{15}$$

where N is the total number of pixels in the image and $p(d_i) = N(d_i) / \sum_{i=1}^p N(d_i)$. Note that the mean detection rate RD as defined by Eq. (14) is the average of the detection rates for all detected objects; similarly, the mean false alarm rate RF as defined by Eq. (15) is the average of the false alarm rates for all detected objects. According to Eqs (12)–(15), each fixed a% can generate a pair of RD and RF . Furthermore, increasing a% from 0% to 100% gradually can generate a set of pairs (RD , RF). In this experiment, we adopted the method proposed in [14] of plotting the ROC curves of (RD , RF). Fig. 3 shows the ROC curves of the CEM and KFLM, respectively, for SNR = 5, 15, 25 and 35dB. The ROC curves in Fig. 3 provide the mean detection rate versus the mean false alarm rate of the classifier. As seen in Fig. 3, the performance of the CEM is excellent when SNR = 25 and 35dB, and degrades when SNR is decreased. From Fig. 3, we can see that CEM has better performances in each kind of SNR than KFLM.

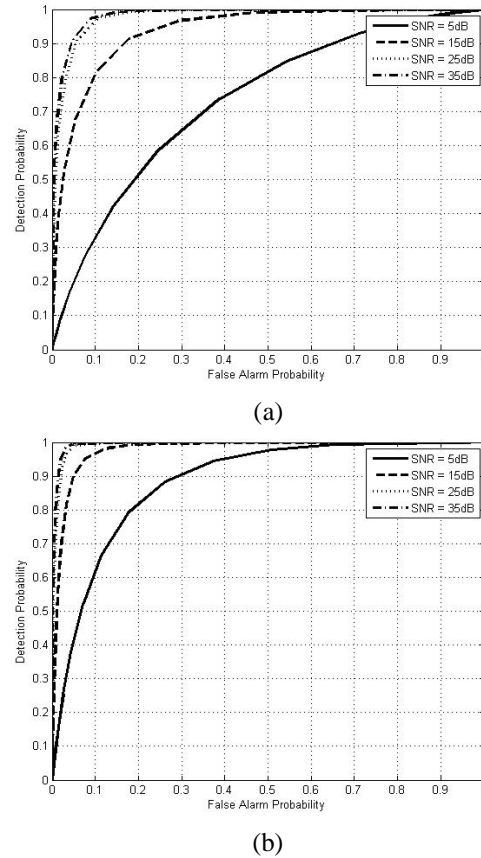


Figure 3: Receiver Operating Characteristic (ROC) curves of (a) KFLM and (b) CEM, in computer-simulated phantoms with different SNRs.

To compare the classification performance of the CEM with that of the KFLM and CM method, we further define the Correct Classification Rates (Rc) for a particular object signature as follows:

$$R_c = \frac{N_D(\mathbf{d}_i) + N_N(\mathbf{d}_i)}{N} \quad (16)$$

where $NN(\mathbf{d}_i)$ represents the number of pixels that are not specified by the i -th object signature \mathbf{d}_i and classified into non-object pixels accurately. Table 2 tabulates the calculated Rc of the CEM, KFLM and CM methods for targeting the detection object on the tumor, and Table 3 is for all major tissues (Fatty, Glandular, Muscle and Tumor) respectively with different SNRs, from which we can see that the CEM performs better than the KFLM and CM method with an appropriate choice of $a\%$, especially, for high-noise images, which conforms to the characteristics of breast MRIs.

Table 2: Correct Classification Rates (Rc) of the CM, KFLM and CEM for tumor only.

SNR	5dB	15dB	25dB	35dB
CM	0.77339	0.83372	0.87645	0.92931
KFLM	0.807019 ($a\%=65\%$)	0.883675 ($a\%=55\%$)	0.957267 ($a\%=50\%$)	0.965388 ($a\%=50\%$)
CEM	0.882238 ($a\%=45\%$)	0.988199 ($a\%=40\%$)	0.998939 ($a\%=30\%$)	0.999355 ($a\%=30\%$)

Table 3: Correct Classification Rates (Rc) of the CM, KFLM and CEM for all major tissues.

SNR	5dB	15dB	25dB	35dB
CM	0.769532	0.862935	0.88278	0.90975
KFLM	0.754959 ($a\%=60\%$)	0.862656 ($a\%=50\%$)	0.915772 ($a\%=50\%$)	0.927771 ($a\%=45\%$)
CEM	0.807342 ($a\%=45\%$)	0.921402 ($a\%=35\%$)	0.956523 ($a\%=25\%$)	0.966741 ($a\%=25\%$)

5.2 Real MRI Experiments

In the following experiments, real breast MRIs acquired from patients with abnormal pathologies were used for the performance evaluation. All MR examinations were performed with a 1.5-T clinical imager (Magnetom Vision plus; Siemens, Erlangen, Germany or Signa Excite HDx; GE Healthcare, Milwaukee, Wis). One sagittal section of 2 cases is shown in Fig. 4, with four different sequences which were selected from Flash (fast low-angle shot gradient echo sequence), T1 (T1-weighted image), T2 (T2-weighted image), PD (proton density image), T1_FS (T1-weighted fat-saturated image), T2_FS

(T2-weighted fat-saturated image) or PD_FS (proton density fat-saturated image). Moreover, the two cases also present different breast sizes and lesion sizes. In many breast MRI applications, fatty tissue, glandular tissue, tumor and muscle are the tissues of major interest, and knowledge of these tissues can generally be obtained directly from the images. In our experiments, the spectral signatures of the four major interest tissues required for the CM, KFLM and CEM approach were extracted directly from breast MRIs and verified by experienced radiologists, as shown in Fig. 5, which was also used for sampling the average gray level values and the variance of the tissues in each band for the computer-simulated phantoms in previous sections.

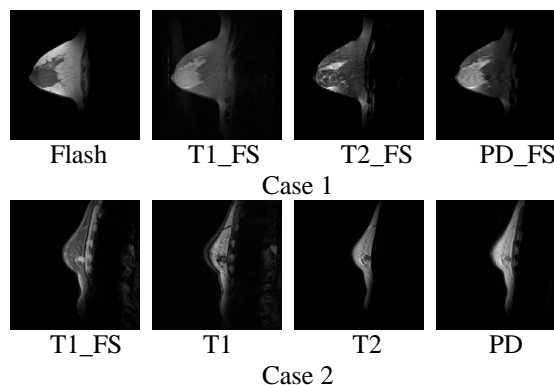


Figure 4: Two cases of real breast MRI. In each case, four different sequences were selected.

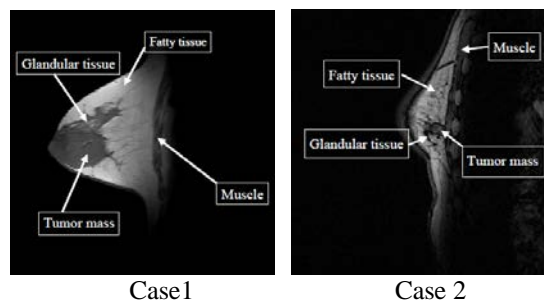


Figure 5: Four major tissues verified by experienced radiologists.

It is a well-established fact that malignant lesions release angiogenic factors that increase local vessel density and vessel permeability. Accordingly, in dynamic contrast-enhanced breast MR imaging, breast cancers are detectable due to their strong enhancement that peaks early after a contrast material injection. Figs. 6(a)–(c) show dynamic contrast-enhanced breast MRIs with the subtraction, acquired by subtraction of the images before and after the injection of contrast material at different lengths of time (1 minute, 3 minutes and 5 minutes after intravenous administration of the contrast agent, respectively) for 2 cases. Figs 7(a)–(d) show the high contrast images resulting from using the KFLM and CEM approach on Fig. 4. It can be seen that the object tissues in the images generated by the CEM are of greater contrast and accuracy than KFLM.

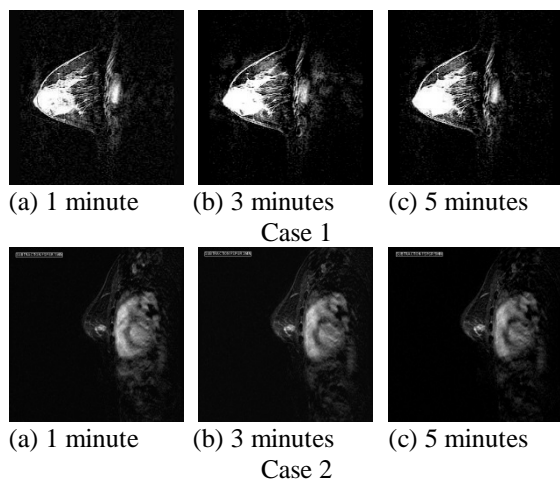


Figure 6: Real breast MRIs acquired by contrast injection in 2 cases.

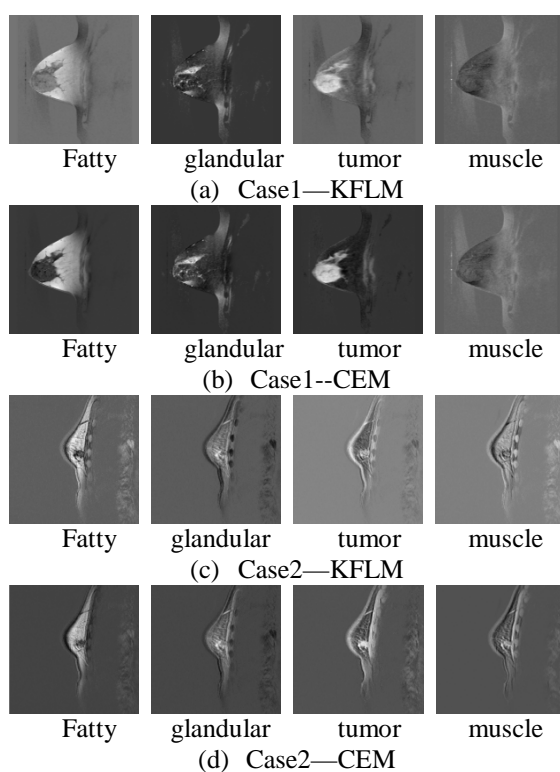


Figure 7: High-contrast images acquired by using the KFLM and CEM method, the detection objects were targeted on four major tissues.

6. Conclusions

This study proposed the CEM, a spectral signature detection technology based on spectral analysis to classify major tissues, for contrast enhancement in breast MRI. In classical spatial-based pattern classification, the data are required to be classified into a number of pattern classes, and for those algorithms based on shape and feature analysis are unreliable due to the changeability of the soft tissues.

The CEM approach remedies those flaws by extracting the objects of interest while effectively minimizing interfering effects resulting from unknown signal sources which include background sources. It was based on a premise that no background information is required for the target detection. More specifically, the only working knowledge for the CEM is the desired target. This advantage is particularly significant when the desired targets are present in an image with complicated background that involves many unknown and unidentified targets which are not of our interest. In MRI classification, it often occurs that interested objects are known a priori while complete knowledge of the image background may not be available due to its complexity resulting from variabilities of tissues characterization.

The experiment results indicate the promising possibilities of this proposed approach. After comparing with the Kalman filter-based linear mixing method – KFLM, common used spatial-based pattern classification method – CM, the CEM approach has been proven to have better quality and is able to correctly classify the breast MRIs into high contrast tissue-separated images from four sequences of non-injected breast MRIs. We anticipate that these tissue-separated images may become an alternative other than the contrast injection to help radiologists in the diagnosis of breast tumors.

Acknowledgments

The work was supported by the Ministry of Science and Technology, Taiwan, under the Grant No. MOST 103-2221-E-167-025.

References

- [1]. Rene Gilles, Jean-Marc Guinebretiere, Olivier Lucidarme, Philippe Cluzel, Gilbert Janaud, Jean-Francois Finet, Anne Tardivon, Jacques Masselot, Daniel Vanel, "Nonpalpable Breast Tumors: Diagnosis with Contrast-enhanced Subtraction Dynamic MR Imaging" *Radiology*; 191:625-631, 1994.
- [2]. Christiane Katharina Kuhl, Rita K. Schmutzler, Claudia Christiane Leutner, Andrea Kempe, Eva Wardelmann, Andrea Hocke, Monika Maringa, Ulrich Pfeifer, Dieter Krebs and Hans Heinz Schild, "Breast MR Imaging Screening in 192 Women Proved or Suspected to be Carriers of a Breast Cancer Susceptibility Gene: Preliminary Results1" *Radiology*; 215:267-279, 2000.

- [3]. S. Heywang-Kobrunner and R. Beck, "Contrast-enhanced MRI of the breast", 2nd edition, Springer-Verlag, 1996.
- [4]. Wiginton, C. D., B. Kelly, A. Oto, M. Jesse, P. Aristimuno, R. Ernst and G. Chaljub. Gadolinium-based contrast exposure, nephrogenic systemic fibrosis, and gadolinium detection in tissue. *AJR Am J Roentgenol*; 190(4):1060-1068, 2008.
- [5]. R. S. Resmini, M. E. Kappus, W. S. Aldrich, J. C. Harsanyi, and M. Anderson, "Mineral mapping with HYperspectral Digital Imagery Collection Experiment (HYDICE) sensor data at Cuprite, Nevada, U.S.A.," *Int. J. Remote Sensing*, vol. 18, no. 17, pp. 1553–1570, 1997.
- [6]. W. Farrand and J. C. Harsanyi, "Mapping the distribution of mine tailing in the Coeur d'Alene river valley, Idaho, through the use of constrained energy minimization technique," *Remote Sensing of Environment*, vol. 59, pp. 64–76, 1997.
- [7]. Chuin-Mu Wang, Clayton Chi-Chang Chen, Yi-Nung Chung, Sheng-Chih Yang, Pau-Choo Chung, Ching-Wen Yang, and Chein-I. Chang, "Detection of Spectral Signatures in Multispectral MR Images for Classification" *IEEE Trans. on Medical Imaging*, Vol. 22, No. 1, January 2003.
- [8]. Sheng-Chih Yang, Chuin-Mu Wang, Hsian-He Hsu, Pau-Choo Chung, Giu-Cheng Hsu, Chun-Jung Juan, Chien-Shun Lo, "Contrast Enhancement and Tissues Classification of Breast MRI Using Kalman Filter-based Linear Mixing Method", *Computerized Medical Imaging and Graphics*, Vol. 33, No. 3, pp. 187-196, April 2009.
- [9]. Chang, C.-I and C. Brumby, "A Kalman filtering approach to multispectral image classification and detection of changes in signature abundance," *IEEE Trans. on Geoscience and Remote Sensing*, vol. 37, pp. 257-268, Jan. 1999.
- [10]. S. Haykin, *Adaptive Filtering Theory*, 3rd ed. Englewood Cliffs, NJ: Prentice-Hall, 1996.
- [11]. R. Schalkoff, *Pattern Recognition: Statistical, Structural and Neural Approaches*. New York: Wiley, 1992.
- [12]. R. O. Duda and P. E. Hart, *Pattern Classification and Scene Analysis*. New York: Wiley, 1973.
- [13]. C.-I. Chang and H. Ren, "An experiment-based quantitative and comparative analysis of hyperspectral target detection and image classification algorithms," *IEEE Trans. Geosci. Remote Sensing*, vol. 38, pp. 1044–1063, Mar. 2000.
- [14]. C. E. Metz, "ROC methodology in radiological imaging," *Investigat Radiol.*, vol. 21, pp. 720–723, 1986.



Sheng-Chih Yang received his MS degree in Computer and Information Science from Knowledge System Institute (KSI), Illinois, U.S.A. in 1996 and Ph.D. degree in Electrical Engineering from National Cheng Kung University (NCKU), Taiwan, in 2006. From 1996 to 2005, he worked as a lecturer at the Department of Electronic Engineering, National Chin Yi University of Technology (NCUT), and is an associate professor at the Department of Computer Science and Information Engineering since 2006. He was the director of Computer Center of NCUT, from 2008 to 2013. His research interests include image processing and biomedical image processing.



Dong-Yuan Wu received the B.S. degree in Computer Science and Information Engineering from National Chin Yi University of Technology (NCUT), Taiwan, in 2014. He is currently a graduate student of the Department of Computer Science and Information Engineering, National Chin-Yi University of Technology. His research interests are image processing and medical image analysis.